Journal of Materials Chemistry A

ROYAL SOCIETY OF CHEMISTRY

PAPER

View Article Online
View Journal | View Issue

Cite this: *J. Mater. Chem. A*, 2025, **13**, 31623

A dual-stabilization strategy for tubular zinc-iodine flow batteries

Ifeanyi Emmanuel Udom, Yan Yao* and Lihong Zhao *

Zinc-iodine flow batteries offer a sustainable, aqueous-based solution for grid-scale energy storage, with tubular cell design further offering enhanced power density. However, non-uniform Zn deposition remains a critical barrier to long-term stability. Here, we report a dual-stabilization strategy that combines geometrical electrode modification with electrolyte engineering to stabilize Zn metal deposition. Geometrically, a tri-helical Zn anode architecture redistributes the electric field and homogenizes current density, promoting uniform deposition. Chemically, the NH_4Br additive modulates the zinc-ion solvation structure through NH_4^+ and captures free iodine species with Br^- to inhibit polyiodide shuttling. Electrochemical impedance spectroscopy confirms reduced interfacial resistance and diffusion impedance, with dense and uniform Zn deposition in the dual-modified system. The approach enables over 350 stable charge–discharge cycles at 10 mA cm^{-2} with coulombic efficiencies exceeding 98% in a tubular cell and allows high-rate cycling up to 72 mA cm^{-2} under full discharge and charge conditions, outperforming cells with only geometrical or chemical modification. This work demonstrates that coupling anode geometry and electrolyte engineering effectively mitigates persistent failure modes in tubular Zn–I_2 systems, offering a viable pathway toward safer and longer-lasting flow batteries for large-scale energy storage.

Received 10th June 2025
Accepted 3rd August 2025

DOI: 10.1039/d5ta04678e

rsc.li/materials-a

Department of Electrical and Computer Engineering, Texas Centre for Super Conductivity, University of Houston, Houston, Texas, USA. E-mail: yyao4@central.uh.edu; lzhao26@central.uh.edu

Lihong Zhao

Lihong Zhao is an Assistant Professor in the Department of Electrical and Computer Engineering at the University of Houston. He received his B.S. in Materials Science and Engineering from Tsinghua University (2014) and PhD from the University of Illinois at Urbana-Champaign (2020). His research focuses on the electro-chemo-mechanics of cathode materials, metal anode mechanics, operando characterization, and machine learning in battery diagnostics. Dr Zhao has first-authored multiple publications in journals including Nat. Commun., Adv. Energy Mater., and ACS Energy Lett. He is a recipient of the 2025 Ralph E. Powe Junior Faculty Enhancement Award.

Introduction

Grid-scale energy storage is essential for integrating variable renewable energy sources into modern power grids. Among emerging technologies, aqueous zinc-iodine flow batteries (ZIFBs) offer a promising solution owing to their low cost, inherent safety, and environmental compatibility. Zinc is naturally abundant and non-toxic and possesses a high theoretical capacity of 820 mAh g^{-1},[1,2] making it an attractive anode material for stationary applications.[1] Traditional aqueous redox flow batteries (RFBs), including all-vanadium and iron–chromium systems, typically exhibit energy densities below 25 Wh L^{-1}.[3–6] The limited energy density arises from both their low cell voltages constrained by water electrolysis and the modest solubility of their redox-active species that limits capacity.[6–8] ZIFBs employ aqueous electrolyte with a near-neutral pH and avoid corrosive or toxic components.[7–9] The redox couples $Zn^{2+}|Zn$ (−0.76 V *vs.* SHE) and $I_3^-|I^-$ (+0.53 V *vs.* SHE) provide an open-circuit cell voltage of approximately 1.29 V,[10,11] offering higher energy density and safer chemistry. Zn–I_2 flow batteries have demonstrated energy densities up to 167 Wh L^{-1} by employing ambipolar high concentration electrolytes that maximize active materials content while minimizing inactive solvent volume.[6]

Despite these advantages, ZIFBs face major durability challenges. Zn deposition tends to be non-uniform,[12] especially on planar electrodes. Uneven electric fields concentrate current at

the electrode edges,[11,13] promoting localized zinc deposition.[14,15] As cycling proceeds, deposition inhomogeneity exacerbates, eventually leading to separator penetration and short-circuiting.[16] In the meantime, iodide (I^-) oxidation to triiodide (I_3^-) during charging introduces additional challenges. I_3^- is soluble and diffuses across the separator,[17] where it reacts parasitically with the Zn metal anode, accelerating corrosion and self-discharge.[18] This polyiodide crossover, exacerbated by hydraulic pressure imbalance and convective transport through porous separators, has been identified as a dominant capacity fading mechanism in ZIFBs.[19] While strategies such as separator or interface engineering mitigate these effects, these strategies often sacrifice ionic conductivity, thus limiting the power density.[20] Consequently, many planar ZIFB systems suffer from rapid capacity fade, especially during high-rate cycling.[21,22]

Tubular battery architecture has emerged as a promising alternative (Fig. 1a) to overcome the current inhomogeneity of planar electrode designs. Their cylindrical symmetry improves current distribution and increases surface area, promoting more uniform plating and reducing local field intensities.[16,20,21] An initial tubular design using a single Zn wire achieved decent power density but with a limited state of charge and low areal capacity to mitigate dendritic growth and preserve stability.[23] In our previous work, we found that a single wire cannot sustain uniform Zn deposition over extended cycling. We developed a tri-helical zinc anode composed of three tightly twisted Zn wires to overcome this challenge.[22] This structure balances radial electric fields[24] and increases the electroactive surface area, effectively mitigating non-uniform plating and enabling stable cycling for over 200 cycles.

Nonetheless, chemical degradation of the Zn wire remains a concern, particularly at the zinc-electrolyte interface. Side reactions corrode the anode surface and compromise mechanical integrity.[16,25–27] To address this challenge, electrolyte additives such as NH_4Br have been introduced. Ammonium ions modulate the Zn^{2+} solvation structure, mitigate side reactions from the aqueous solvent sheath and stabilize metal deposition.[21] Meanwhile, Br^- coordinates with iodine, forming I_2Br^- complexes that reduce shuttle effects.[21] Recent studies show that these additives suppress Zn dendritic growth in aqueous systems and extend cycle life.[28,29] Asymmetric electrolyte formulations have also been proposed to suppress water migration and enhance redox stability under dynamic flow conditions.[30] However, most research on additives has focused on planar cells, and the effects of additives in tubular geometries, where transport dynamics and field symmetry differ, remain underexplored.

Here, we show that a dual-stabilization strategy, combining geometric and chemical approaches, significantly enhances Zn plating stability in tubular ZIFBs, even under high-current and deep-charging conditions. Geometrically, the tri-helical electrode design reduces peak current density and suppresses non-uniform deposition. Chemically, the NH_4Br additive promotes uniform zinc plating and mitigates corrosion of the Zn wire anode, preventing catastrophic cell failure. Together, these advances establish a scalable design framework for safe, high-performance, and durable flow battery systems for grid-scale energy storage.

Experimental methods

Cell configuration and materials

A tubular Zn–I_2 flow battery was constructed using a custom cylindrical housing with a tri-helical zinc anode, as shown in Fig. S1.[22] The anode consists of three high-purity zinc wires (99.95%, $\Phi = 0.25$ mm) uniformly twisted into a tightly wound helix, as both the electrode and the current collector. A cation-exchange membrane (Nafion TT-030, Perma Pure) separated the anolyte and catholyte. The tubular membrane has an internal diameter of 0.64 mm and a wall thickness of 0.076 mm and was cut to a length of 24 cm, corresponding to an internal volume of 0.31 cm^3. The membrane was thoroughly rinsed and soaked in deionized water before use. Both tube terminals were sealed using chemically resistant epoxy to prevent leakage. Inside the

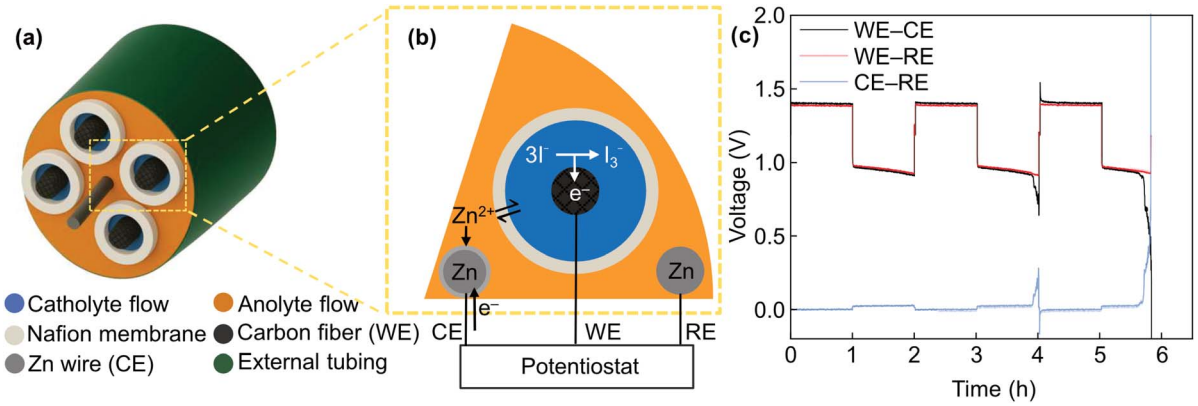

Fig. 1 Schematic of a tubular Zn–I_2 flow battery and origin of cell failure characterized by a three-electrode test. (a) Schematic of the tubular Zn–I_2 flow cell employing a single cylindrical zinc anode. (b) Enlarged view of the electrode structure, electrochemical reactions during charging, and the three-electrode configuration to evaluate the origin of failure. An additional Zn wire was used as a reference electrode (RE) to measure the potentials of the working electrode (WE) and the counter electrode (CE) during cycling. (c) Electrode potential of the tubular cell. Rapid increase in CE potential during discharge (Zn stripping) represents corrosion-induced electrode breaking and subsequent open circuiting.

catholyte compartment, a porous carbon fiber bundle was inserted along the full membrane length to serve as the cathode current collector and provide a high surface area for the I_3^-/I^- redox reaction. All tubing, fittings, and enclosures were made from polytetrafluoroethylene (PTFE) because of its chemical resistance to iodine species.

Electrolyte formulations

The baseline electrolyte comprised 2.0 mol L^{-1} ZnI_2 (Sigma-Aldrich) dissolved in deionized water. Electrolyte with an additive included an additional 2.0 mol L^{-1} NH_4Br (Sigma-Aldrich, ≥99%) or KBr (Alfa Aesar, 99%) in both the anolyte and catholyte reservoirs. The additive increased ionic conductivity from 17.3 S m^{-1} to 24.0 S m^{-1} at 25 °C (Fig. S2).

Flow cell operation

Electrolytes were circulated at a rate of 30 mL min^{-1} using a dual-channel peristaltic pump (Masterflex) to maintain consistent flow. For each test, 6 mL of anolyte and 6 mL of catholyte were used per cell.

Electrochemical testing

Galvanostatic cycling was performed using a Biologic SP300 potentiostat at 25 °C. Cells were charged and discharged between 0.20 and 2.00 V *vs.* Zn^{2+}/Zn. For longevity tests, a current density of 10 mA cm^{-2} was applied. Deep charge–discharge performance was evaluated at current densities of 36 mA cm^{-2} and 72 mA cm^{-2}. Three-electrode tests were conducted to examine potential variation at each electrode. An additional Zn wire was used as a reference electrode in the identical tubular battery setup. For linear sweep voltammetry (LSV) experiments, the coin cell with the Zn|electrolyte|stainless steel structure was scanned at 0.5 mV s^{-1}. Glass fiber (Whatman GF-A) was used as the separator.

UV-Vis characterization

Ultraviolet-visible (UV-Vis) absorption spectra were collected using an Agilent Cary 60 spectrometer. After charging 6 mL of ZnI_2-based electrolyte for 10 mAh, the electrolyte was diluted by a factor of 500 to 3000 to bring the I_3^- absorption peak within the linear response range. The measured spectra were then rescaled based on the dilution factor to recover the original absorption profile. The alignment of the shoulder near 250 nm across all samples indicates consistent I^- concentration (I^- absorption is at 227 nm), serving as an internal reference for normalization.[31]

Electrochemical impedance spectroscopy (EIS)

EIS measurements were conducted at a 10 mV amplitude from 1 MHz to 100 mHz. All measurements were collected after 10 minutes of rest to ensure stabilization. The spectra were further analyzed using the Distribution of Relaxation Times (DRT) method to deconvolute impedance contribution from the solution, interface, and mass transport.[32–34]

Post-mortem analysis

After cycling, zinc electrodes were removed, rinsed with deionized water, and dried in air. Optical images were collected with a Keyence VHX-X1 microscope. Cross-sections were prepared by Ar^+ beam polishing (JEOL, IB-10520CCP) at 25 °C and 8 kV. Scanning electron microscopy (SEM) images and energy-dispersive spectroscopy (EDS) were collected with a Thermo Scientific Axia SEM.

Electric field modelling

Electric field modeling was carried out with the finite-difference method in MATLAB. A 7.5 mm × 7.5 mm simulation domain was discretized into a 151 × 151 grid. Three circular zinc wires (radius 0.5 mm) were arranged in a tri-helical configuration with nearly zero spacing. The Laplace equation ($\nabla^2 V = 0$) was solved using a Gauss–Seidel relaxation algorithm over 750 iterations. To simulate electrochemical operation, the wire regions were held at 1 V, while the domain boundary was grounded, allowing evaluation of field-driven deposition behaviour.

Results and discussion

Tri-helical electrode design to mitigate Zn corrosion

In a tubular ZIFB, the redox reactions proceed similarly to those in planar configurations, as illustrated in Fig. 1b. During charging, Zn^{2+} cations are reduced and plated on the tri-helical Zn anode, while I^- is oxidized to I_3^- in the catholyte. The half-cell reactions are expressed as

$$\text{Negative: } Zn \rightarrow Zn^{2+} + 2e^-$$

$$\text{Positive: } I_3^- + 2e^- \rightarrow 3I^-$$

These reactions explain the charge storage mechanism, with visible changes in catholyte color shifting from clear to dark brown (Fig. S3), indicating I_3^- formation.

Unlike in planar ZIFBs that suffer from dendrite-induced short-circuiting, the cycling instability of tubular cell architecture originates from Zn wire corrosion and subsequent electrode disconnection that leads to open-circuiting, consistent with failure modes caused by Zn corrosion in related systems.[28,35,36] To identify the failure behavior in conventional tubular Zn–I_2 cells, we monitored the electrochemical potential of both working and counter electrodes with a three-electrode setup in Fig. 1c at 10 mA cm^{-2}. During cycling, the working electrode potential remained relatively stable. In contrast, the counter electrode potential rapidly increased during discharge in the second cycle and resulted in catastrophic failure in the 3rd cycle. The stable working electrode potential indicates the absence of short-circuiting in tubular cell architecture. Indeed, the rapid increase in counter electrode potential represents a drastic increase in the electronic resistance of the anode caused by Zn wire corrosion and loss of the electron-conducting pathway along the Zn wire, as evidenced by Fig. S4. These early

failures are representative of corrosion-induced breakdown under non-uniform field conditions. Our previous work integrated multiple Zn wires into the electrode design to increase the surface area and reduce the effective current density, thereby extending the cycle life of tubular Zn flow batteries.[21]

In addition to the increased surface area provided by the tri-helical design compared to the single-wire setup, we found that the close contact between Zn wires also helped reduce electric field inhomogeneity around the anode. Finite difference modeling of the electric field distribution, shown in Fig. 2a–d, was used to evaluate whether alternative anode geometries could lower localized current density gradients and mitigate dendrite-prone hotspots. To ensure a fair comparison, a configuration of three spaced Zn wires (3× cylindrical) with the same total cross-sectional area as the tri-helical design was included. In practice, such a design often suffers from uneven wire spacing, which can further exacerbate field inhomogeneity.

In the 3× cylindrical Zn anode, the electric field is distributed around each individual wire, resulting in a broad and scattered intensity profile along the radial direction, as shown in Fig. 2e. The electric field values exhibit a large standard deviation (indicated by the error bar) and widely separated minimum and maximum values (red dashed lines). This uneven distribution promotes random Zn deposition in broad high-intensity regions, increasing the likelihood of non-uniform plating.

In contrast, when the three wires are tightly wound in the tri-helical design (Fig. 2f), the electric field intensity peaks at the outer envelope of the Zn wire cross-section and decays exponentially along the radial direction. The high-intensity region is confined to a narrow zone adjacent to the Zn surface, promoting zinc deposition within a well-defined area and minimizing the risk of non-uniform growth. Even with a slightly reduced surface area compared to the 3× cylindrical Zn anode cell (Fig. S5), the tri-helical geometry can mitigate field-driven deposition instabilities by acting as a built-in current distributor.[21,28,37]

Effect of additives on zinc deposition in tubular cells

While the tri-helical architecture effectively reduces electric field inhomogeneity and promotes uniform zinc deposition, further stabilization requires chemical modulation of the electrolyte to mitigate interfacial reactions and suppress corrosion. To date, most additive studies have focused on conventional ZIFBs with planar Zn electrodes. Here, we evaluate the effect of electrolyte additives in the context of a tubular tri-helical Zn electrode. Specifically, we investigate NH_4Br, a widely studied additive in Zn–I_2 systems,[21] to understand how a well-studied chemical modifier influences zinc plating stability with a novel cell architecture. Together, the architectural and electrolyte modifications serve as a dual-pronged strategy towards the major degradation pathways in Zn–I_2 flow systems.

The role of the NH_4Br additive is illustrated in Fig. 3a. Bromide ions complex with iodine intermediates (I_2Br^-), limiting uncontrolled polyiodide formation and suppressing iodine shuttling.[37] The suppression is supported by UV-Vis

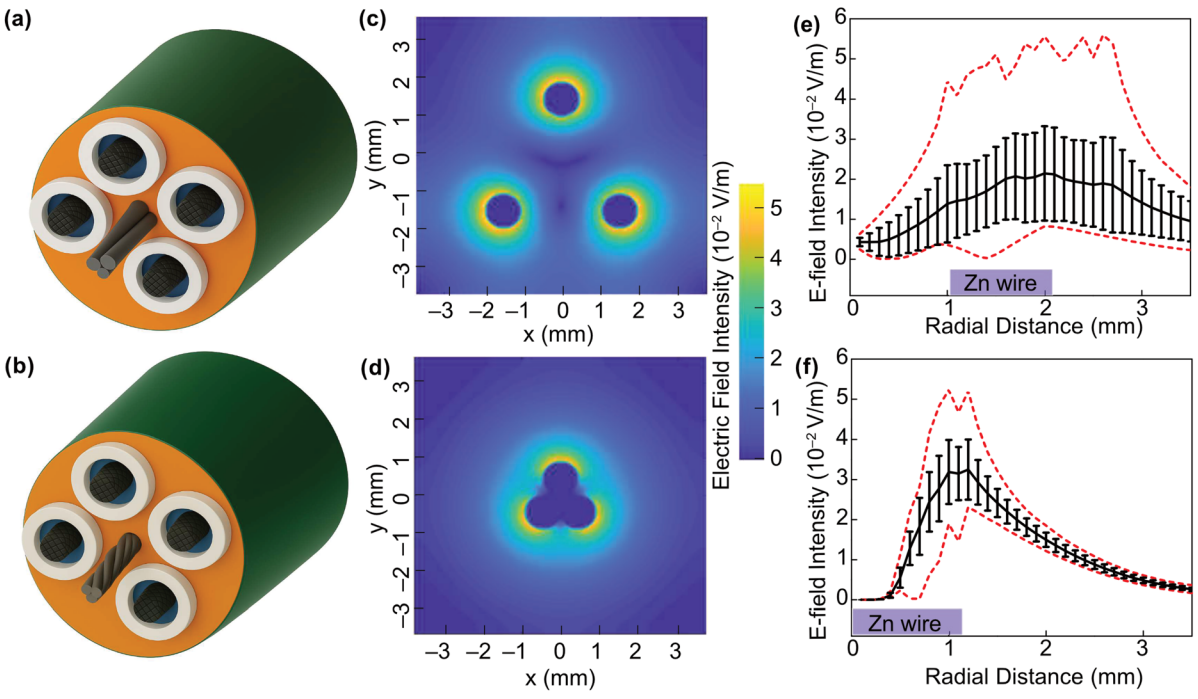

Fig. 2 Electric field distribution in the tubular Zn–I_2 flow battery. Schematic of (a) the 3× cylindrical Zn anode and (b) the tri-helical Zn anode. (c) Electric field intensity and distribution of (c) the 3× cylindrical Zn anode and (d) the tri-helical Zn anode. (e) Radial electric field intensity in the vicinity of (e) the 3× cylindrical Zn anode and (f) the tri-helical Zn anode. Black line and error bar represent the average and standard deviation of intensity values, while red dashed lines represent maximum and minimum values. Zero-intensity regions corresponding to the internal of the Zn wire are excluded from the calculation. Purple box with the "Zn wire" represents the location of the Zn wire in the radial direction.

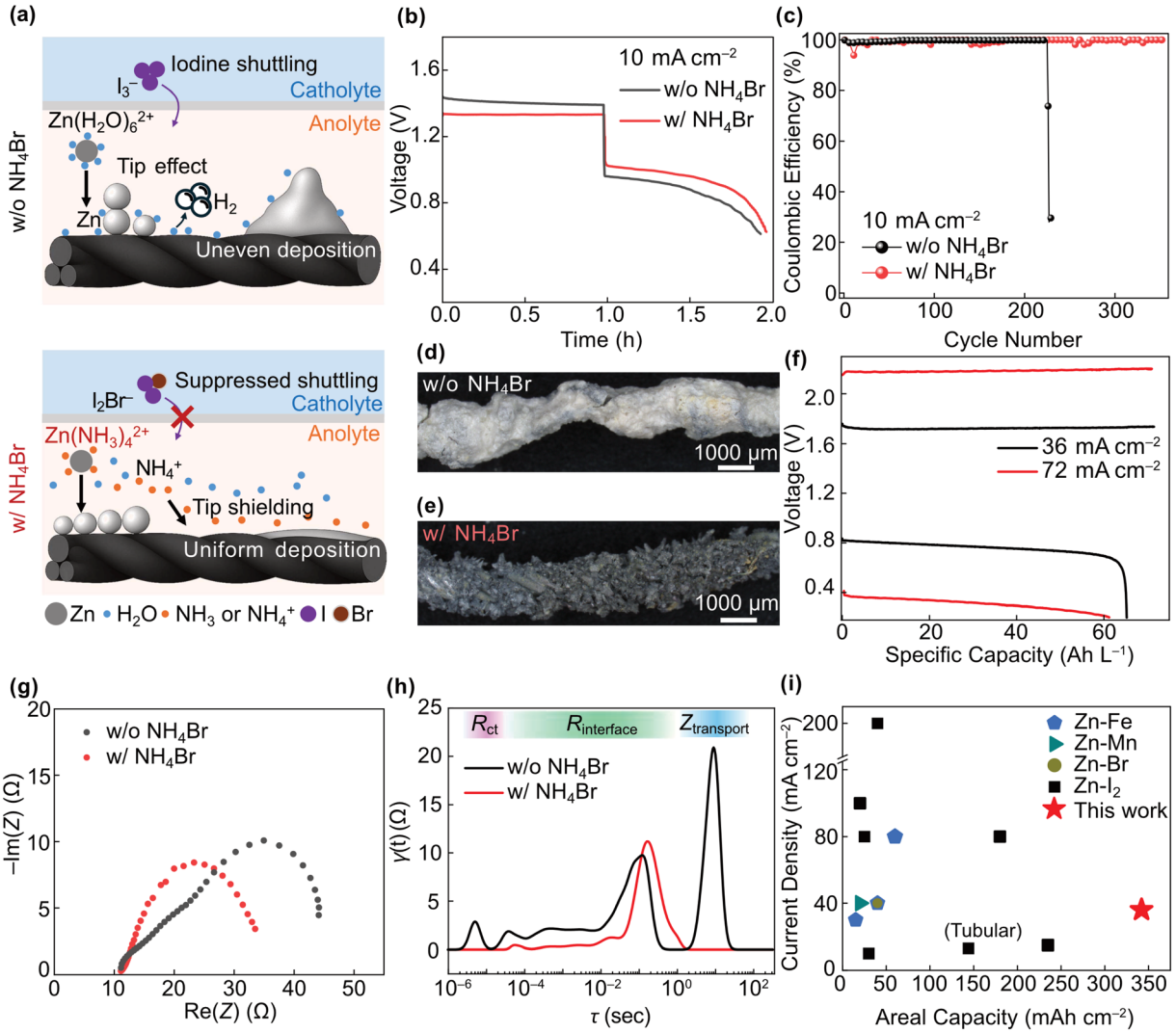

Fig. 3 Electrochemical characterization of the tri-helical Zn–I_2 flow battery with and without the NH_4Br additive. (a) Schematic showing the role of the NH_4Br additive in tri-helical tubular Zn–I_2 batteries. (b) Voltage profiles at 10 mA cm^{-2} for a single cycle with (black) and without (red) NH_4Br. (c) Coulombic efficiency over cycles at 10 mA cm^{-2}. Optical image of the tri-helical Zn anode (d) after 220 cycles without the additive and (e) 350 cycles with NH_4Br. (f) Voltage profile at 36 and 72 mA cm^{-2} and full 100% depth-of-discharge. (g) Nyquist plot and (h) DRT profile of the full cell at the pristine state. (i) Benchmarking cell current density and areal capacity with reported Zn flow batteries.

analysis (Fig. S6). In the presence of Br^-, the characteristic I_3^- absorption peaks at 288 nm and 351 nm exhibit significantly low intensity in the catholyte, and no I_3^- signal is detected in the anolyte. Fig. S6c shows that the anolyte containing Br^- remains optically clear after charging, in sharp contrast to the red-brown anolyte observed in the control sample, which indicates iodine shuttling. These results confirm that Br^- effectively complexes with I_2 species and inhibits their cross-diffusion, thereby enhancing long-term cycling stability.

NH_4^+ cations can adsorb onto the Zn surface, forming an electrostatic shielding layer that suppresses the hydrogen evolution reaction (HER), a contributor to capacity loss and anode corrosion.[38] This mechanism is further supported by *ex situ* X-ray absorption spectroscopy analysis reported by Tangthuam *et al.*, which revealed NH_4^+-mediated interfacial stabilization and HER suppression in Zn–I_2 electrolytes.[39] The addition of NH_4Br results in a decreased cell overpotential by approximately 65 mV in both charge and discharge processes (Fig. 3b). In contrast, the addition of Br^- alone *via* KBr does not significantly affect the cell overpotential (Fig. S7), suggesting that the improvement primarily stems from the presence of NH_4^+. To solidify this claim, we conducted LSV to measure the HER onset potential in ZnI_2 electrolyte with and without NH_4^+. As shown in Fig. S8, the HER onset shifts to a more negative potential by 0.12 V in the presence of NH_4^+, confirming suppressed HER kinetics.

The dual-stabilization translates to improved electrochemical performance, with the NH_4Br-containing cell achieving an average coulombic efficiency of 98% and an average energy efficiency of 78% at 10 mA cm^{-2} cycling. As shown in Fig. 3c, the cell without NH_4Br exhibits a rapid drop in coulombic efficiency after approximately 220 cycles, attributed

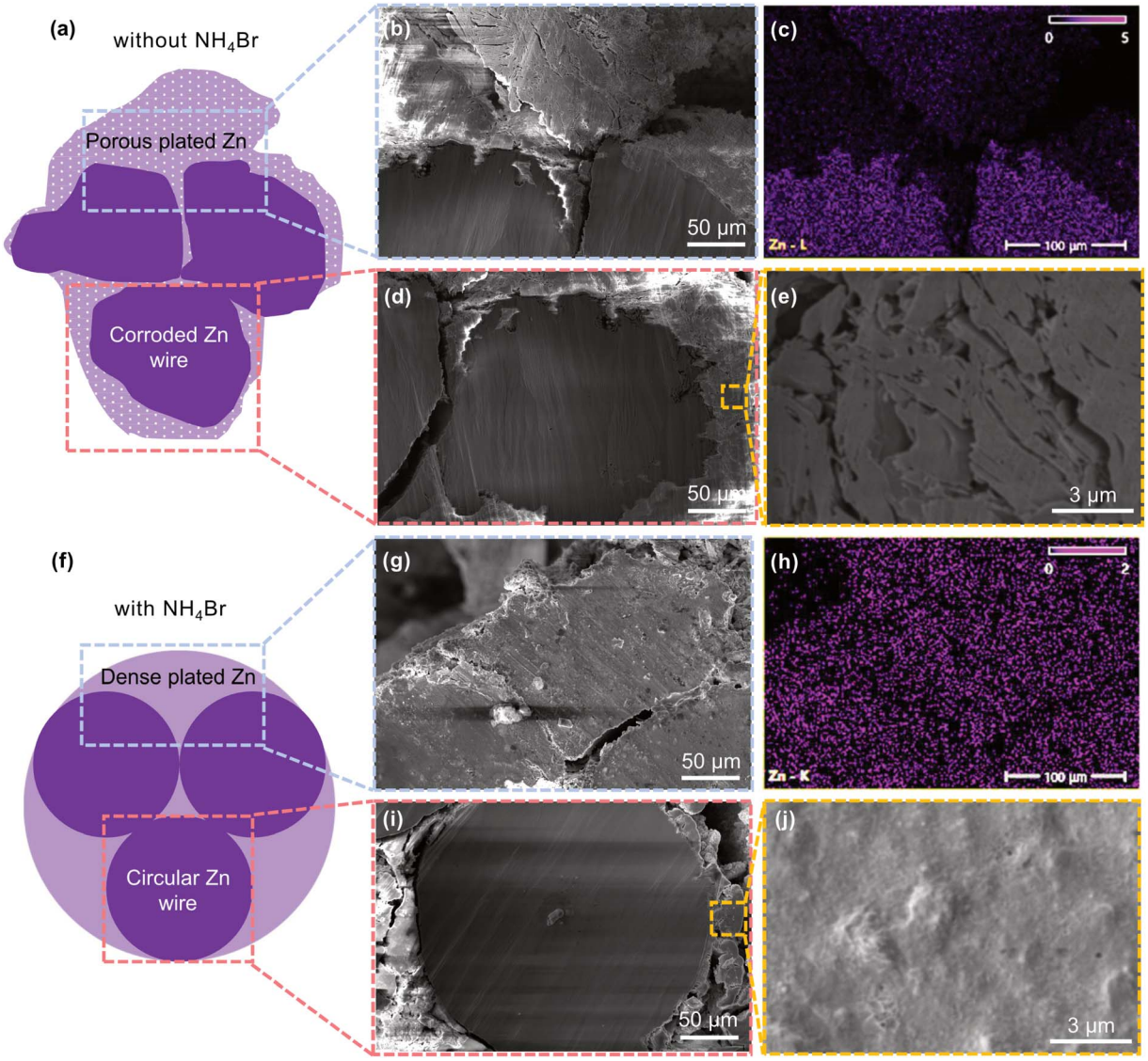

Fig. 4 Postmortem analysis of Zn wire anodes cycled with and without NH_4Br. (a) Schematic of the Zn wire after cycling without NH_4Br, with non-uniform and porous Zn plating and Zn wire corrosion. (b) Cross-sectional SEM image and (c) Zn elemental mapping of Zn plated between two Zn wires without the additive. (d) SEM of the Zn wire after cycling, with the shape deformed and the edge corroded. (e) Zoomed-in image of plated Zn showing a porous structure. (f) Schematic of the Zn wire after cycling with NH_4Br, with uniform and dense Zn plating. (g) Cross-sectional SEM image and (h) Zn elemental mapping of Zn plated between two Zn wires with the additive. (i) SEM of the Zn wire after cycling, with the circular shape retained and a smooth edge. (j) Zoomed-in image of plated Zn showing a dense structure.

to increased parasitic reactions and mechanical degradation of the Zn anode. In contrast, the NH_4Br-containing cell maintains a coulombic efficiency above 98% for over 350 cycles, with no observable capacity decay.

Optical images of tri-helical Zn anodes were taken after 220 cycles without an additive and 350 cycles with an additive. After cycling without an additive, the Zn wire exhibits a matte white color (Fig. 3d). The white color persists even after 24 hours in water, suggesting that the color does not originate from salt residues. This appearance is likely due to the porous nature of the Zn deposits causing diffusive reflection, which will be further validated *via* SEM later. In addition to the abnormal surface color, the Zn anode exhibited a substantial thickness variation (830 μm) along the wire, and in some regions, complete mechanical breakage was observed. Such non-uniform plating and stripping result in loss of electrical connection along the Zn wire and cell failure. In contrast, the Zn anode cycled with the NH_4Br additive retained a metallic color and exhibited a cleaner plating morphology. This denser deposition likely preserved the metallic appearance and mechanical integrity of the Zn wire. The envelope thickness deviation was significantly reduced from 400 μm, indicating much more uniform Zn deposition (Fig. 3e).

The impact of NH_4Br becomes more pronounced at high current densities under deep cycling conditions (Fig. 3f). The cell with the additive delivers nearly 95% of its theoretical

capacity (71 Ah L^{-1}) at 36 mA cm^{-2} and 100% state-of-charge, achieving an energy efficiency of 46%. Even at an extreme current density of 72 mA cm^{-2}, the cell still survives full cycling and exhibits 89% of its theoretical capacity. In contrast, cells without additives exhibited a large overpotential and could not be cycled within the electrochemical stability window of ZIFB electrolytes (Fig. S9). The improved performance at high rates and deep charge levels is attributed to enhanced Zn plating kinetics and morphology and increased ionic conductivity provided by the additive. At deep charge states, when ZnI_2 is nearly depleted, NH_4Br helps preserve ionic conductivity, which reduces overpotential and mitigates dendritic growth by alleviating mass transport limitations.

The interfacial kinetics are further probed by EIS at the charged state after 100 cycles in the cell, as shown in Fig. 3b. Nyquist plots (Fig. 3g) show that both cells have similar *x*-axis intercepts, indicating comparable solution resistance. The cell without NH_4Br exhibits an additional semicircle in the medium-frequency range, suggesting hindered interfacial kinetics. To better interpret EIS data, we performed a DRT analysis to decouple contributions from different components in Fig. 3h. The cell without an additive exhibited an additional peak at around 10^{-5} seconds, corresponding to the extra semicircle near 10^5 Hz in the Nyquist plot, likely due to increased charge transfer resistance.[32,40,41] Both cells showed similar DRT profiles within the 10^{-5}–10^0 second range, suggesting a similar interface resistance that arises from the identical tri-helical cell configuration. At low frequencies ($\sim 10^1$ seconds), the cell without the additive exhibits an extra peak corresponding to diffusion, indicating mass transport limitations due to ZnI_2 depletion at a high state of charge. In contrast, diffusion-associated impedance is negligible in cells with NH_4Br. Impedance analysis aligns with the cycling results, highlighting the additive's role in enhancing interfacial kinetics and maintaining effective mass transport at high states of charge.

To benchmark our system against existing aqueous Zn-based chemistries, we compared areal capacities and current densities across Zn–Fe, Zn–Br, and Zn–I_2 systems (Fig. 3i and Table S1).[11] Our geometrically and chemically stabilized tubular Zn–I_2 system (red star) achieves a remarkable total areal capacity of 340 mAh cm^{-2} at a current density of 36 mA cm^{-2}, exceeding previously reported values for tubular configurations (13.1 mA cm^{-2})[23] as well as a planar cell configuration. While some planar systems operate at higher current densities, they often suffer from lower areal capacities due to limited layer-to-layer distance and non-uniform Zn plating into a separator.[17] The dual-stabilization strategy within a tubular cell architecture enables simultaneous high areal capacity and large current densities, offering a performance advantage over planar ZIFB systems.

Postmortem analysis was performed to correlate the electrochemical performance with morphological evolution at the Zn anode. Fig. 4 compares the cross-sectional morphology and elemental distribution for tri-helical Zn anodes cycled with and without the NH_4Br additive. Without the additive, Zn plating appears porous and highly non-uniform (Fig. 4a). The deposited Zn exhibits an irregular shape (Fig. 4b), poor adhesion to the wire substrate, significant delamination, and weaker EDS intensity relative to the pristine Zn wire (Fig. 4c), indicating a lower density structure (Fig. 4e). Irregular plating and stripping also induced localized corrosion of the original wire. As shown in Fig. 4d, the corroded Zn wire exhibited a reduced circularity of 0.45 and visible pitting along the perimeter, contributing to mechanical failure and eventual cell breakdown.

In contrast, the Zn anode cycled with NH_4Br shows uniform and dense Zn plating (Fig. 4f). The plated Zn remains conformal to the wire substrate, with relatively minor separation (Fig. 4g). Elemental mapping reveals a homogeneous Zn distribution, with EDS intensity comparable to the Zn wire substrates (Fig. 4h), indicating a compact structure that is further confirmed by the zoomed-in image in Fig. 4j. The Zn wire maintains a high circularity of 0.92. This robust morphology supports the enhanced cycling stability observed electrochemically.

Conclusion

In this work, we present a dual-stabilization strategy to address key limitations in zinc–iodine tubular flow batteries, particularly Zn wire breakage caused by non-uniform plating and stripping. Geometrically, the tri-helical structure guides Zn deposition to more desirable locations compared to conventionally spaced Zn wires. Chemically, the addition of NH_4Br promotes uniform and dense Zn plating. This combined approach enables over 350 stable cycles with coulombic efficiencies exceeding 98%, along with reduced charge transfer and transport impedance. Our results highlight the critical role of coupling electrolyte chemistry with electrode architecture and establish a scalable platform for durable, high-performance Zn–I_2 flow batteries suitable for grid-scale energy storage.

From a system-level perspective, the tubular cell format is fully compatible with conventional redox flow battery hardware, including peristaltic pumps, Nafion-based membranes, and cylindrical enclosures. As it requires no new manufacturing infrastructure, the tri-helical Zn anode design and NH_4Br-containing electrolyte can be readily integrated into existing or retrofitted systems.

Nevertheless, several practical considerations remain. These include the long-term stability of Zn wire electrodes, total electrolyte cost at scale, and membrane durability over extended operation. In particular, the high cost of iodide and bromide salts may present a barrier to large-scale implementation. Future efforts should focus on life-cycle analysis, stack-level integration, and additive screening for enhanced durability, as well as membrane optimization for extended service life.

Author contributions

L. Z and Y. Y. directed the project. I. U. designed and performed the experiment and wrote the manuscript. L. Z., and Y. Y. revised the manuscript.

Conflicts of interest

The authors declare no competing interests.

Data availability

The data supporting this article have been included as part of the SI.

Supplementary information contains Fig. S1–S9 and Table S1, covering cell configuration, conductivity measurement, optical and UV-vis characterization of electrode and electrolyte, supplementary voltage profile, and benchmark of cycling performance. See DOI: **https://doi.org/10.1039/d5ta04678e**.

Acknowledgements

L. Z. acknowledges the University of Houston for the new faculty start-up fund. Y. Y. acknowledges the financial support from the Texas Center for Superconductivity at the University of Houston. I. E. U. acknowledges the UH Chevron Energy Graduate Fellows Award (2025).

References

1 A. Konarov, N. Voronina, J. H. Jo, Z. Bakenov, Y.-K. Sun and S.-T. Myung, Present and future perspective on electrode materials for rechargeable zinc-ion batteries, *ACS Energy Lett.*, 2018, **3**(10), 2620–2640, DOI: **10.1021/acsenergylett.8b01552**.

2 D. Lin and Y. Li, Recent advances of aqueous rechargeable zinc-iodine batteries: challenges, solutions, and prospects, *Adv. Mater.*, 2022, **34**(23), 2108856, DOI: **10.1002/adma.202108856**.

3 M. Skyllas-Kazacos, M. H. Chakrabarti, S. A. Hajimolana, F. S. Mjalli and M. Saleem, Progress in flow battery research and development, *J. Electrochem. Soc.*, 2011, **158**(8), R55, DOI: **10.1149/1.3599565**.

4 A. Z. Weber, M. M. Mench, J. P. Meyers, P. N. Ross, J. T. Gostick and Q. Liu, Redox flow batteries: a review, *J. Appl. Electrochem.*, 2011, **41**(10), 1137–1164, DOI: **10.1007/s10800-011-0348-2**.

5 P. Leung, X. Li, C. Ponce De León, L. Berlouis, C. T. J. Low and F. C. Walsh, Progress in redox flow batteries, remaining challenges and their applications in energy storage, *RSC Adv.*, 2012, **2**(27), 10125, DOI: **10.1039/c2ra21342g**.

6 B. Li, Z. Nie, M. Vijayakumar, G. Li, J. Liu, V. Sprenkle and W. Wang, Ambipolar zinc-polyiodide electrolyte for a high-energy density aqueous redox flow battery, *Nat. Commun.*, 2015, **6**, 6303, DOI: **10.1038/ncomms7303**.

7 H. Pan, Y. Shao, P. Yan, Y. Cheng, K. S. Han, Z. Nie, C. Wang, J. Yang, X. Li, P. Bhattacharya, K. T. Mueller and J. Liu, Reversible aqueous zinc/manganese oxide energy storage from conversion reactions, *Nat. Energy*, 2016, **1**(5), 16039, DOI: **10.1038/nenergy.2016.39**.

8 P. H. Svensson and L. Kloo, Synthesis, structure, and bonding in polyiodide and metal iodide–iodine systems, *Chem. Rev.*, 2003, **103**(5), 1649–1684, DOI: **10.1021/cr0204101**.

9 W. Lu, C. Xie, H. Zhang and X. Li, Inhibition of zinc dendrite growth in zinc-based batteries, *ChemSusChem*, 2018, **11**(23), 3996–4006, DOI: **10.1002/cssc.201801657**.

10 Z. Wei, Z. Huang, G. Liang, Y. Wang, S. Wang, Y. Yang, T. Hu and C. Zhi, Starch-mediated colloidal chemistry for highly reversible zinc-based polyiodide redox flow batteries, *Nat. Commun.*, 2024, **15**, 3841, DOI: **10.1038/s41467-024-48263-8**.

11 C. Wang, G. Gao, Y. Su, J. Xie, D. He, X. Wang, Y. Wang and Y. Wang, High-voltage and dendrite-free zinc-iodine flow battery, *Nat. Commun.*, 2024, **15**(1), 6234, DOI: **10.1038/s41467-024-50543-2**.

12 W. Yu, W. Shang, Y. He, Z. Zhao, Y. Ma and P. Tan, Unraveling the mechanism of non-uniform zinc deposition in rechargeable zinc-based batteries with vertical orientation, *Chem. Eng. J.*, 2022, **431**, 134032, DOI: **10.1016/j.cej.2021.134032**.

13 Q. Jian, J. Sun, H. Li, Z. Guo and T. Zhao, Phase-field modeling of zinc dendrites growth in aqueous zinc batteries, *Int. J. Heat Mass Transfer*, 2024, **223**, 125252, DOI: **10.1016/j.ijheatmasstransfer.2024.125252**.

14 Z. Song, C. Yang, N. Kiatwisarnkij, A. Lu, N. Tunghathaithip, K. Lolupiman, T. Bovornratanaraks, X. Zhang, G. He and J. Qin, Polyethylene glycol-protected zinc microwall arrays for stable zinc anodes, *ACS Appl. Mater. Interfaces*, 2024, **16**(47), 64834–64845, DOI: **10.1021/acsami.4c15130**.

15 J. Zou, G. Wang, S. Lin, H. Yang, X. Ma, H. Ji, S. Zhu, Y. Lyu, C. Wang, Y. Zhou, Q. He, Q. Wang, F. Gao, Z. Zhang, T. Hao, Z. Wang, Y. Zhang, X. Liu and Y. Wu, A biphasic membraneless zinc-iodine battery with high volumetric capacity, *Adv. Funct. Mater.*, 2024, **34**(51), 2415607, DOI: **10.1002/adfm.202415607**.

16 Z. Chen, Y. Zhao, P. Cui, J. Zhu, X. Gao, G. He and X. Yi, Unidirectional ion sieve enabling high-flux and reversible zinc anodes, *ACS Nano*, 2025, **19**(15), 14987–15001, DOI: **10.1021/acsnano.5c01103**.

17 Y. Zhang, G. Yang, M. L. Lehmann, C. Wu, L. Zhao, T. Saito, Y. Liang, J. Nanda and Y. Yao, Separator effect on zinc electrodeposition behavior and its implication for zinc battery lifetime, *Nano Lett.*, 2021, **21**(24), 10446–10452, DOI: **10.1021/acs.nanolett.1c03792**.

18 C. Xie, H. Zhang, W. Xu, W. Wang and X. Li, A Long cycle life, self-healing zinc–iodine flow battery with high power density, *Angew. Chem., Int. Ed.*, 2018, **57**(35), 11171–11176, DOI: **10.1002/anie.201803122**.

19 M. Mousavi, H. Dou, H. Fathiannasab, C. J. Silva, A. Yu and Z. Chen, Elucidating and tackling capacity fading of zinc-iodine redox flow batteries, *Chem. Eng. J.*, 2021, **412**, 128499, DOI: **10.1016/j.cej.2021.128499**.

20 W. Yan, Y. Liu, J. Qiu, F. Tan, J. Liang, X. Cai, C. Dai, J. Zhao and Z. Lin, A tripartite synergistic optimization strategy for zinc-iodine batteries, *Nat. Commun.*, 2024, **15**, 9702, DOI: **10.1038/s41467-024-53800-6**.

21 Q. P. Jian, M. C. Wu, H. R. Jiang, Y. K. Lin and T. S. Zhao, A trifunctional electrolyte for high-performance zinc-iodine

flow batteries, *J. Power Sources*, 2021, **484**, 229238, DOI: 10.1016/j.jpowsour.2020.229238.

22 I. E. Udom, L. Zhao, Y. Yao and A. E. Lakraychi, Tri-helical anode design for zinc-iodine tubular flow batteries, in *2025 IEEE Electrical Energy Storage Applications and Technologies Conference (EESAT)*, IEEE, Charlotte, NC, USA, 2025, pp. 1–7, DOI: 10.1109/EESAT62935.2025.10891221.

23 Y. Wu, F. Zhang, T. Wang, P.-W. Huang, A. Filippas, H. Yang, Y. Huang, C. Wang, H. Liu, X. Xie, R. P. Lively and N. Liu, A submillimeter bundled microtubular flow battery cell with ultrahigh volumetric power density, *Proc. Natl. Acad. Sci. U. S. A.*, 2023, **120**(2), e2213528120, DOI: 10.1073/pnas.2213528120.

24 J. Xu, H. Li, Y. Jin, D. Zhou, B. Sun, M. Armand and G. Wang, Understanding the electrical mechanisms in aqueous zinc metal batteries: from electrostatic interactions to electric field regulation, *Adv. Mater.*, 2024, **36**(3), 2309726, DOI: 10.1002/adma.202309726.

25 N. Wang, S. Zhai, Y. Ma, X. Tan, K. Jiang, W. Zhong, W. Zhang, N. Chen, W. Chen, S. Li, G. Han and Z. Li, Tridentate citrate chelation towards stable fiber zinc-polypyrrole battery with hybrid mechanism, *Energy Storage Mater.*, 2021, **43**, 585–594, DOI: 10.1016/j.ensm.2021.10.004.

26 S. L. Mallinson, J. R. Varcoe and R. C. T. Slade, Examination of amine-functionalised anion-exchange membranes for possible use in the all-vanadium redox flow battery, *Electrochim. Acta*, 2014, **140**, 145–151, DOI: 10.1016/j.electacta.2014.06.058.

27 M. Mousavi, G. Jiang, J. Zhang, A. G. Kashkooli, H. Dou, C. J. Silva, Z. P. Cano, Y. Niu, A. Yu and Z. Chen, Decoupled low-cost ammonium-based electrolyte design for highly stable zinc–iodine redox flow batteries, *Energy Storage Mater.*, 2020, **32**, 465–476, DOI: 10.1016/j.ensm.2020.06.031.

28 W. Zhong, H. Cheng, S. Zhang, L. Li, C. Tan, W. Chen and Y. Lu, Cation-driven phase transition and anion-enhanced kinetics for high energy efficiency zinc-interhalide complex batteries, *Nat. Commun.*, 2025, **16**(1), 4586, DOI: 10.1038/s41467-025-59894-w.

29 C. Lin, X. Yang, P. Xiong, H. Lin, L. He, Q. Yao, M. Wei, Q. Qian, Q. Chen and L. Zeng, High-rate, large capacity, and long life dendrite-free Zn metal anode enabled by trifunctional electrolyte additive with a wide temperature range, *Adv. Sci.*, 2022, **9**(21), 2201433, DOI: 10.1002/advs.202201433.

30 M. Chakraborty, T. Andreu, B. Molinari, J. R. Morante and S. Murcia-López, Suppressing water migration in aqueous zn-iodide flow batteries by asymmetric electrolyte formulation, *Electrochim. Acta*, 2023, **461**, 142660, DOI: 10.1016/j.electacta.2023.142660.

31 X. Zheng, R. Luo, T. Ahmad, J. Sun, S. Liu, N. Chen, M. Wang, Y. Yuan, M. Chuai, Y. Xu, T. Jiang and W. Chen, Development of high areal capacity electrolytic MnO_2–Zn battery *via* an iodine mediator, *Energy Environ. Eng.*, 2023, **6**(6), e12433, DOI: 10.1002/eem2.12433.

32 T. H. Wan, M. Saccoccio, C. Chen and F. Ciucci, Influence of the discretization methods on the distribution of relaxation times deconvolution: implementing radial basis functions with DRTtools, *Electrochim. Acta*, 2015, **184**, 483–499, DOI: 10.1016/j.electacta.2015.09.097.

33 F. Dion and A. Lasia, The use of regularization methods in the deconvolution of underlying distributions in electrochemical processes, *J. Electroanal. Chem.*, 1999, **475**(1), 28–37, DOI: 10.1016/S0022-0728(99)00334-4.

34 S. Buller, M. Thele, E. Karden and R. W. De Doncker, Impedance-based non-linear dynamic battery modeling for automotive applications, *J. Power Sources*, 2003, **113**(2), 422–430, DOI: 10.1016/S0378-7753(02)00558-X.

35 X. Wang, C. Sun and Z. Wu, Recent progress of dendrite-free stable zinc anodes for advanced zinc-based rechargeable batteries: fundamentals, challenges, and perspectives, *SusMat*, 2023, **3**(2), 180–206, DOI: 10.1002/sus2.118.

36 J. Tao, Q. Chen, Z. Chen, B. Cui, X. Xu, J. Han, R. Yuan, Q. Xu, Y. Peng and H. Liu, Recent advances in interfacial engineering for high-performance zn anodes: challenges, solutions, and prospects, *ACS Appl. Energy Mater.*, 2025, 5c00620, DOI: 10.1021/acsaem.5c00620.

37 G.-M. Weng, Z. Li, G. Cong, Y. Zhou and Y.-C. Lu, Unlocking the capacity of iodide for high-energy-density zinc/polyiodide and lithium/polyiodide redox flow batteries, *Energy Environ. Sci.*, 2017, **10**(3), 735–741, DOI: 10.1039/C6EE03554J.

38 Y. Gong, B. Wang, H. Ren, D. Li, D. Wang, H. Liu and S. Dou, Recent advances in structural optimization and surface modification on current collectors for high-performance zinc anode: principles, strategies, and challenges, *Nano-Micro Lett.*, 2023, **15**(1), 208, DOI: 10.1007/s40820-023-01177-4.

39 P. Tangthuam, S. Wannapaiboon, P. Kidkhunthod, J.-L. Chen, C.-C. Chang, C. W. Pao, P. A. Zijdemans, T. Yonezawa, M. Suttipong and S. Kheawhom, Innovative pH-buffering strategies for enhanced cycling stability in zinc–iodine flow batteries, *J. Mater. Chem. A*, 2024, **12**(43), 29513–29525, DOI: 10.1039/d4ta06102k.

40 K. Köble, M. Schilling, L. Eifert, N. Bevilacqua, K. F. Fahy, P. Atanassov, A. Bazylak and R. Zeis, Revealing the multifaceted impacts of electrode modifications for vanadium redox flow battery electrodes, *ACS Appl. Mater. Interfaces*, 2023, **15**(40), 46775–46789, DOI: 10.1021/acsami.3c07940.

41 M. B. Dixit, J.-S. Park, P. Kenesei, J. Almer and K. B. Hatzell, Status and prospect of *in situ* and *operando* characterization of solid-state batteries, *Energy Environ. Sci.*, 2021, **14**(9), 4672–4711, DOI: 10.1039/D1EE00638J.